

Laser-programmed stiffness and interfaces for textile hybrid electronics

Received: 8 May 2025

Accepted: 24 November 2025

Published online: 13 January 2026

 Check for updates

Huayu Luo ^{1,6}, Zimo Cai ^{1,6}, Geng Yang ¹, Kangjie Ye¹, Jian Tang², Tao Liu¹, Long He ³, Ying Zhang³, Yi Zhu ¹, Haibo Xie^{1,2}, Kewang Nan ⁴, Huayong Yang^{1,2}, Michael D. Dickey ⁵ & Kaichen Xu ¹ ✉

Permeable textiles show great potential for daily wearable electronics. As crucial electronic components, rigid chips suffer from modulus mismatch with elastic textile substrates, hindering the development of stretchable hybrid electronics. Herein, we report laser-programmed textile hybrid electronics (LPTHE) featuring seamless integration of wires and chips onto laser-programmed textiles (LPTs). Through selective and controllable laser-polymer interaction, LPTs are tailored with gradient stiffness and interfacial affinities. The laser-pretreated regions exhibit a modulus increase ranging from 2.7-fold to 14.9-fold, while maintaining permeability and biological safety. Such LPT provides stretch stability to LPTHE, creating strain isolation between rigid chips and elastic textiles, while also protecting wires on textiles from disconnection and cross-layer short circuits. We demonstrate an LPTHE screen with 5×5 light-emitting diodes displaying variable patterns under deformation. Additionally, an untethered stretchable LPTHE patch continuously monitors four health parameters during exercise. The proposed strategy bridges the gap between hybrid electronics and elastic daily textiles.

Textiles with a permeable and durable nature are highly appealing for wearable electronics, with various applications in displays^{1,2}, communication³, energy management^{4,5}, human-machine interfaces^{6,7}, and health monitoring⁸⁻¹⁰. As textile electronics evolve toward increasing functional complexity, components for comprehensive signal conditioning and computation become essential for driving system-level performances¹¹. Semiconductor fibers are promising candidates with both wearing comfort and processing capability, whereas they are currently at an early stage of development without system-level functionality^{12,13}. Alternatively, silicon-based chips are extensively adopted in textile electronic systems, typically mounted on conventional circuit boards as add-on modules. However, such impermeable and inextensible substrates compromise the wearing comfort of textile systems. Hence, the seamless integration of rigid

chips into textiles is of practical significance for developing monolithic and comfortable textile electronic systems¹⁴.

Typical strategies for monolithic textile electronics involve layer-by-layer integration via photolithography¹⁵, embroidery¹⁶, screen printing¹⁷ and transfer printing¹⁸. Planar textile circuits fabricated by these methods can be directly soldered to chips, realizing universal functionalities. In addition, constructing one-dimensional fibers with embedded chips represents another viable approach¹⁹. These strategies primarily rely on inelastic textile substrates, which provide exceptional structural stability and thus protect attached components. Nevertheless, they are not ideal for conformal interfacing with human skin or for acquiring faithful epidermal signals (Fig. 1a). In contrast, elastic textiles (e.g., knitted textiles) offer opportunities for intimate contact between the skin and electronics.

¹State Key Laboratory of Fluid Power and Mechatronics Systems, School of Mechanical Engineering, Zhejiang University, Hangzhou, China. ²Institute of Advanced Machines Zhejiang University, Hangzhou, China. ³Zhiyuan Research Institute, Hangzhou, China. ⁴State Key Laboratory of Advanced Drug Delivery and Release Systems, College of Pharmaceutical Sciences, Zhejiang University, Hangzhou, China. ⁵Department of Chemical and Biomolecular Engineering, North Carolina State University, Raleigh, NC, USA. ⁶These authors contributed equally: Huayu Luo, Zimo Cai. ✉ e-mail: xukc@zju.edu.cn

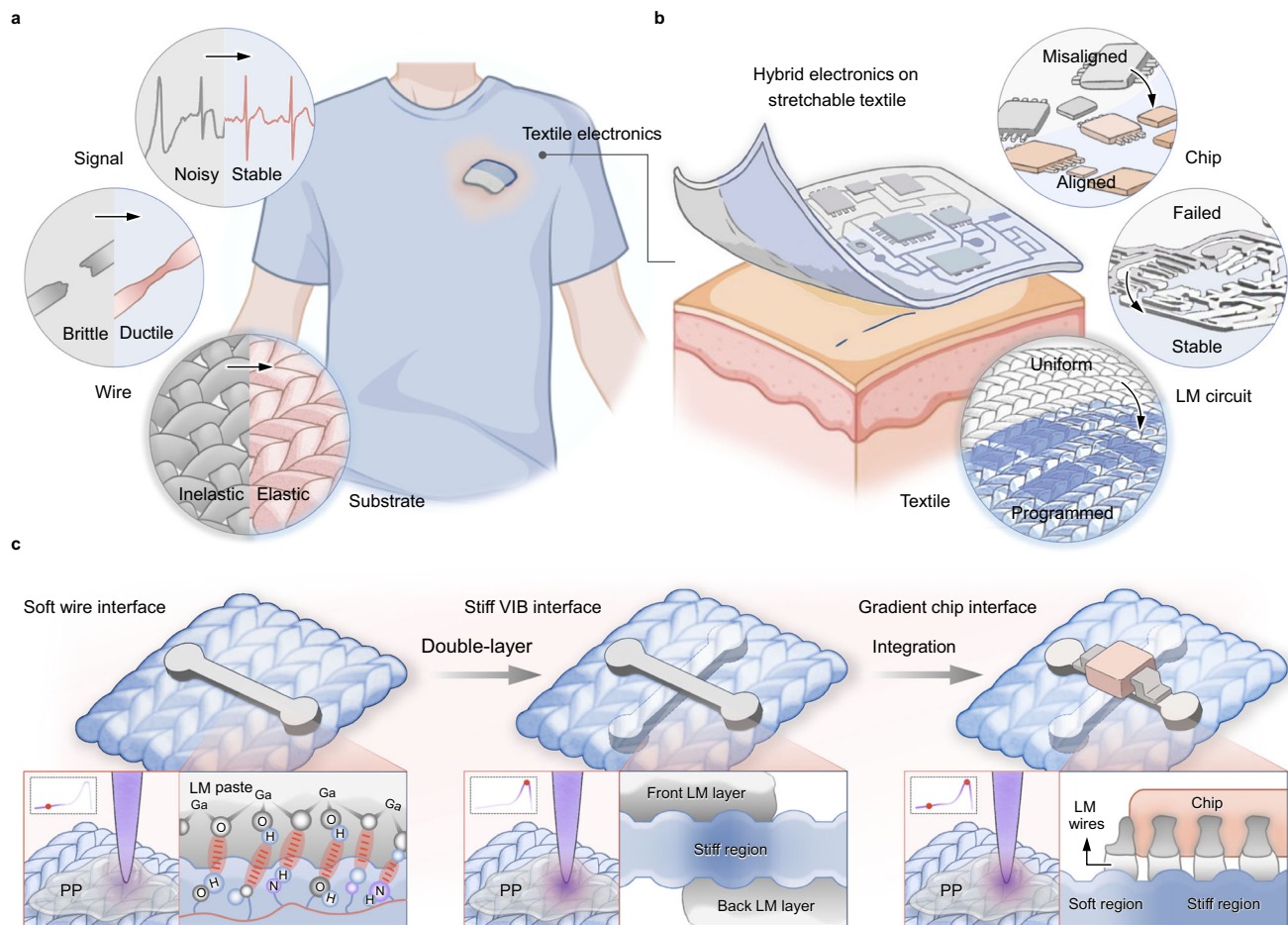


Fig. 1 | Design and principle of laser-programmed textile hybrid electronics.

a Comparisons between textile electronics on elastic and inelastic textile substrates. Elastic textile electronics offer superior mechanical compliance, skin conformability, and reliable signal acquisition from the skin. Inelastic textile electronics, in contrast, face inherent limitations in adapting to skin dynamics, which hinders conformability and signal fidelity. LM, liquid metal. Some elements were created in BioRender. Electronics, F. (2025) <https://BioRender.com/t0yrpvj>. **b** Schematics showing several advantages of programmed textile substrates for

stretchable hybrid electronics. Textiles with spatially programmed stiffness and interfacial affinities reliably interface with hybrid electronic components during stretching. **c** Working principles of the laser-programmed textile for stretchable hybrid electronics. The laser fluence modulates the polymerization of PP infiltrated in textiles, producing chemical groups for hydrogen bonds, as well as programmable stiffness. The curves in the insets represent the relationship between the stiffness and laser fluence. PP, photocurable polymer; VIB vertical interconnect block.

Moreover, liquid metal (LM) with intrinsic fluidity and electrical conductivity are applicable interconnect and solder media for assembling chips on these textiles^{20–22}. However, challenges persist in dynamic and patterned strain distributions on structurally elastic textiles, leading to mechanical mismatch with hybrid electronic components²³. In addition, the stretch stability of interconnects²⁴ and their susceptibility to cross-layer short circuits^{25,26} remain inherent yet frequently overlooked issues on textile substrates. Therefore, a general and facile strategy is required to reconcile the strain distribution and surface properties of textiles with the requirements of universal electronic components.

In this article, we report laser-programmed textile hybrid electronics (LPTHE), featuring an elaborate laser-programmed textile (LPT) with LM circuits and chips (Fig. 1b). By leveraging selective and regulable interactions between the laser and photo-curable polymer (PP), LPTs are tailored with gradient stiffness and interfacial affinities, ensuring a reliable assembly of hybrid electronic components on elastic textiles. The laser-pretreated regions of textiles exhibit a modulus increase ranging from 2.7-fold to 14.9-fold, with desirable biocompatibility and only a modest compromise to permeability. This design creates strain isolation between rigid chips and soft LM/textile interfaces, as well as protects LM wires from disconnections and cross-

layer short circuits. In this way, the LPTHE enables monolithic and elastic hybrid electronics directly on daily textiles.

Using this technique, we create an LPTHE screen with a 5×5 light-emitting diode (LED) array, displaying variable patterns under multiple deformations. Additionally, an untethered and wearable LPTHE patch is developed that can withstand strains of up to 50% and dynamically monitor human health parameters (electrocardiography (ECG), temperature, humidity and acceleration) during exercise, without causing skin irritation or sweat accumulation. The proposed LPTHE provides a reliable approach toward monolithic and stretchable textile electronic systems, empowering wearable electronics for real-life applications.

Results

Design of the LPT and LPTHE

Light fluence determines the degree of polymerization of PP, thus changing its physical properties²⁷. Based on this mechanism, an ultraviolet (UV) laser, with spatially modulated fluence, interacts with PP precursor infiltrated into the textile matrix (Fig. 1c). In this way, LPTs are endowed with tailored stiffness and interfaces in selective regions.

Depending on specific demands, the interactions between the laser and textiles induces three distinct effects. First, to realize stable conductive traces on stretched textiles, the laser programs soft PP

through partial polymerization, after which LM wires composed of LM/Cu intermetallics²⁸ (denoted as LM pastes) can be deposited on LPTs using stencil printing. Such PP provides interfacial affinities between LM pastes and LPTs by surface smoothing and hydrogen bonding. In addition, soft PP retains the ductile nature of stretchable textiles. Second, to prevent cross-layer short circuits through porous textile substrates, the laser programs fully polymerized PP with a higher stiffness. This relatively stiff PP forms a vertical interconnect block (VIB) at the overlapping regions of front and back LM layers. Such VIB mechanically reinforces the textile, resisting compressive strain and preventing leakage of LM pastes, as well as consequent short circuits along the vertical direction. Third, to bridge the mechanical mismatch between rigid chips and stretchable textiles, the laser programs gradient PP at the textile-chip interfaces. The stiff region beneath the footprint of the chip isolates the strain between soft textile circuits and non-stretchable chips, thus ensuring a reliable connection between LM wires and chips.

The gradient substrate strategy stabilizes rigid/soft interfaces, offering protection against strains along both pin-extension and pin-pitch directions (Supplementary Fig. 1a). Another elastic solder strategy, although it works well in specific scenarios^{20,29–32}, is vulnerable to short circuits under strains along the pin-pitch direction (Supplementary Fig. 1b). Despite the performance of gradient stiffness, its implementations typically involve multistep and selective deposition of stiffening agents^{33–35}, with regions of contrasting stiffness integrated via covalent bonding or mechanical interlocking^{36,37} (Supplementary Tables 1 and 2). These methods are incompatible with textiles due to uncontrolled capillary infiltration of liquid agents, resulting in imprecise reinforcement patterns. The developed LPT features a single-step modification of localized stiffness on textiles, along with enhanced interfacial affinity, while preserving air permeability and biocompatibility. Such an approach simultaneously addresses interfacial mismatches along textiles, interconnects and chips without introducing significant manufacturing complexity. Additionally, the laser programming is mask-free, highly tunable, and can be extended to common polymer films³⁸. Hence, the LPTHE provides opportunities for stretchable hybrid electronic systems on daily textile platforms.

Characterizations of the LPT

Considering the applicability in everyday wearable scenarios, this study focuses on knitted textiles, particularly the weft-knitted spandex fabrics. For PP, a formulation containing polyurethane acrylate as a key component is selected as the precursor, owing to its broad applicability, commercial availability, and processability³⁹. Capillary action promotes thorough infiltration of the PP precursor into the textile matrix, facilitating intimate bonding upon polymerization. The results from nuclear magnetic resonance (NMR), gas chromatography–mass spectrometry (GC–MS), X-ray fluorescence (XRF) and Fourier transform infrared (FTIR) spectroscopy indicate the formation of a co-crosslinked polyurethane-acrylate network in the final polymer (Supplementary Note 1, Supplementary Fig. 2, 3, and Supplementary Table 3). Following that, textiles are washed with isopropanol (IPA) to remove any remaining soluble substances, including the unreacted precursor, as well as any toxic residues trapped in the polymerized regions.

A critical issue lies in the permeability of PP-infiltrated textiles, as uncontrolled infiltration introduces excessive PP precursor, which is retained by hierarchical and open capillary pores in textiles⁴⁰, completely blocking all gaps. By employing an approach of selective liquid retention (SLR), the PP precursor within superficial large gaps is effectively removed (Supplementary Fig. 4 and 5a, b), resulting in permeable textiles after the polymerization of PP. Although some liquid is lost in the SLR process (Supplementary Fig. 5c), the mass increments of PP-infiltrated textiles relative to original ones still show acceptable reproducibility (Fig. 2a).

Photos and scanning electron microscope (SEM) images of the textile selectively infiltrated with PP reveal clear pores under stretching (Fig. 2b and Supplementary Fig. 6). Although residual PP may slightly reduce permeability, the overall porous structure of the textiles is largely retained. Nevertheless, textiles with excessive PP are completely clogged. Membrane pressure tests confirm that the permeability of PP-infiltrated textiles processed via SLR largely matches that of the original textiles (Supplementary Fig. 7). Compared with textiles containing excessive PP, those treated with SLR exhibit a strength reduction, as demonstrated in tensile tests (Fig. 2c, d). Nevertheless, the stiffness of both textiles is significantly higher than that of the original textiles, since PP at the yarn interlacement points, specifically in internal gaps and superficial tiny gaps, restricts the opening of slip knots (Supplementary Fig. 8). Therefore, textiles with selectively infiltrated PP precursor serve as ideal candidates for LPT, balancing permeability and mechanical reinforcement.

For selective polymerization with controllable fluences, a laser is employed as the light source for LPT. Out of the focused laser spot, the relatively rough surface of textiles scatters light and results in localized laser speckle (Fig. 2e). Such laser speckle may compromise the resolution of laser pretreatment. To quantify this effect, a finite-difference time-domain (FDTD) simulation is performed. Relative field intensities are illustrated for the cases where a Gaussian beam is incident on a flat surface and on a textile yarn (Fig. 2f, g). For the textile yarn, although the scattered field of the laser speckle extends across the entire simulation domain, the high-intensity region remains concentrated within the yarn body. By comparing the average Poynting flux in both scenarios, it is found that the majority of the laser power is confined within a diameter of approximately 50 μm (Fig. 2h). Narrow slots engraved by this laser speckle further validate the centralized energy distribution (Supplementary Fig. 9). Given that the dimensions of standard chips and the target width of LM wires are typically greater than 500 μm , the laser speckle is sufficiently localized to program textile interfaces for these electronic components.

Owing to the porosity of textiles, laser scanning from one side enables energy penetration to the opposite side, polymerizing the PP on both sides. Although dye-based characterization suggests a slightly different polymerization degree (Supplementary Fig. 10), FTIR spectroscopy confirms no significant disparity between both sides (Supplementary Fig. 11). One possible explanation is that the silicone board beneath textiles during laser processing reflects UV light, thereby promoting polymerization on the back side. Given that knitted textiles do not exhibit pronounced strain disparities between two sides under structural heterogeneity⁴¹, minor stiffness differences between the two sides are negligible for practical use.

Photos of laser speckles at varied incident powers provide an intuitive visualization of laser interaction with textiles (Fig. 2i and Supplementary Fig. 12). To achieve effective polymerization without ablation, laser parameters must be carefully chosen. Although laser fluence can be technically modulated by laser power alone (Supplementary Note 2), higher powers produce distinct ablation even at short processing durations (Supplementary Fig. 13a, b). In contrast, employing the minimum power (~21.5 mW when active) is critical to prevent net heat accumulation⁴². This low power, in turn, necessitates a slower scanning speed to deliver the required fluence. This longer processing duration matches the polymerization kinetics⁴³, promoting a more effective polymerization (Supplementary Fig. 13c, d). Therefore, the laser power is fixed at its minimum value with the scanning speed adjusted within a relatively slow range.

To quantify the minimum programmable area on PP-infiltrated textiles, stiff regions of various sizes are patterned via the laser direct writing (Fig. 2j). After laser pretreatment, the unpolymerized precursor outside the programmed region can be washed away, while the polymerized PP in the programmed region remains (Supplementary

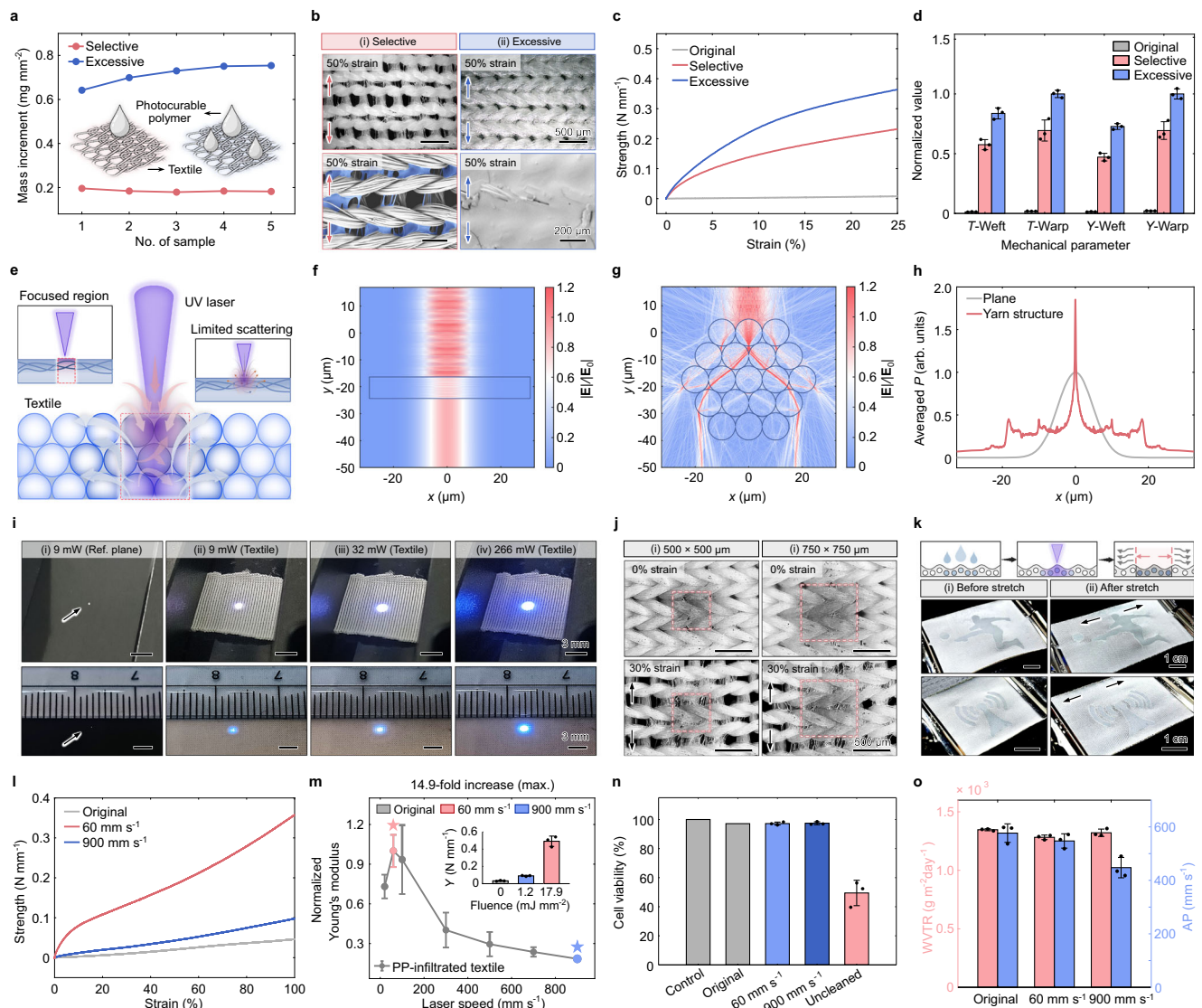


Fig. 2 | PP-infiltrated textile programmed by laser. **a** Mass increment between PP-infiltrated textile and original textiles ($10 \times 10 \text{ mm}^2$). **b** Photos and SEM images of textiles with varied amounts of PP. The bottom left image is presented in false color, with the PP between the yarns colored blue. Images shown are representative of 5 independent replicates, all of which exhibit similar morphology. **c** Strength-strain curves of textiles with varied amounts of PP. Strength denotes force per unit width. **d** Mechanical parameters of textiles with varied amounts of PP. T toughness; Y Young's modulus. Error bars are presented as mean \pm SD for $n = 3$ independent experiments. **e** Schematics showing the formation of laser speckle on textiles. UV, ultraviolet. FDTD simulations of electric field strength where a Gaussian beam is incident onto **(f)** a plane and **(g)** a textile yarn. E_0 : electric field strength of incident beam. **h** Average Poynting flux in the plane and yarn along the horizontal axis. P Poynting flux. **i** Photos of laser speckles on textiles under varied laser powers. **j** Photos showing the minimum polymerized region by laser. The dashed lines

indicate the boundaries of laser pretreatment. **k** Photos showing LPTs with various patterns at the strain of 20%. LPT, laser-programmed textile. **l**, **m** **(l)** Representative strength-strain curves and **(m)** Young's modulus of PP-infiltrated textiles programmed by lasers at varied scanning speeds. Asterisks indicate the selected laser parameters used for fabricating LPTs and LPTHE. Y : Young's modulus. Laser power: 21.5 mW; Line spacing: $40 \mu\text{m}$. Error bars are presented as mean \pm SD for $n = 3$ independent experiments. **n** Cytotoxicity of PP-infiltrated textiles programmed by lasers at varied scanning speeds. The 'uncleaned' sample is processed at a laser speed of 900 mm s^{-1} . Control and original: a single sample is analyzed due to sample uniformity; Others: error bars are presented as mean \pm SD for $n = 3$ independent experiments. **o** Air permeability and water vapor transmission rate of PP-infiltrated textiles programmed by lasers at varied scanning speeds. AP, air permeability; WVTR, water vapor transmission rate. Error bars are presented as mean \pm SD for $n = 3$ independent experiments.

Fig. 14). When stretching these textiles, no noticeable deformation occurs in the programmed region with the length of $750 \mu\text{m}$. However, the $500 \mu\text{m}$ square, more comparable in size to the spacing between yarn interlacement points ($\sim 264 \mu\text{m}$), undergoes significant deformation. This insufficient strength is likely attributed to the non-uniform interlacement of yarns within such a small area^{44,45}. Hence, a minimum characteristic length of $750 \mu\text{m}$ is recommended for effectively stiff regions. To account for variations in chip size and assembly tolerances, all stiff regions in this study are designed with dimensions exceeding $800 \mu\text{m}$, which is compatible with the aforementioned mechanical

requirement. Using laser programming, stiff regions of customized geometries can be fabricated on textiles (Fig. 2k).

By regulating the laser speed in programmed regions, gradient polymerization and corresponding stiffness can be achieved. Textile strips fully scanned by the laser under different speeds are characterized. Strength-strain curves, Young's moduli and toughness values at various laser speeds are presented (Fig. 2l, m, and Supplementary Fig. 15). In the range of 60 to 900 mm s^{-1} , the higher laser speeds result in relatively low degrees of polymerization, and consequently reduced textile stiffness. When the laser speed reaches

1100 mm s⁻¹, the strength of the textile shows minimal difference compared to that programmed at 900 mm s⁻¹ (Supplementary Fig. 16). In contrast, at the laser speed lower than 60 mm s⁻¹, excessive fluence may inhibit polymerization, resulting in reduced textile stiffness. Therefore, laser speeds of 60 and 900 mm s⁻¹ are established as the lower and upper thresholds for effectively programming textiles with gradient stiffness (Supplementary Movie 1). These speeds correspond to fluences of 17.9 and 1.2 mJ mm⁻², respectively (Fig. 2m). Compared with the original textiles (modulus: 33.0 N m⁻¹; toughness: 0.6 N m⁻¹), the PP-infiltrated textiles exhibit 2.7–14.9 times higher modulus (up to 491.8 N m⁻¹) and 3.5–20.8 times greater toughness (up to 13.3 N m⁻¹).

To ensure comfort during long-term wear, the biocompatibility of PP-infiltrated textiles is enhanced through post-polymerization washing. Immersion in IPA induces swelling of the PP network, thereby promoting the leaching of toxic substances such as unreacted monomers and photoinitiators^{46,47}. As a result, cleaned textiles programmed at varied laser speeds exhibit minimal cytotoxicity and superior biocompatibility, with cell viabilities consistently exceeding 95% (Fig. 2n and Supplementary Fig. 17). In contrast, uncleaned textiles demonstrate pronounced toxicity, with cell viabilities falling below 50%, indicating both the effectiveness and necessity of the washing process. The FTIR spectral changes before and after washing demonstrate that

residues are successfully removed from the polymer (Supplementary Fig. 18). Owing to the loss of these substances, the strength of washed PP-infiltrated textiles is insensitive to further UV exposure (Supplementary Fig. 19). This feature is highly beneficial for the long-term preservation of the gradient stiffness on textiles. In addition, PP-infiltrated textiles programmed at these laser speeds retain desirable air and water vapor permeability, comparable to that of original textiles (Fig. 2o). In sum, these findings highlight LPT as a promising strategy for wearable electronics that maintains both biological safety and breathability.

LPT-LM interfaces for stretchable and double-layer circuits

LM and its composites with intrinsic fluidity and conductivity are widely employed as interconnects in stretchable electronics. However, LM wires on textiles are subject to complex strains due to the unique structure of textiles. For a continuous LM wire, only a portion is in direct contact with textile yarns, while the remainder is suspended between them (Fig. 3a and Supplementary Fig. 20a–e). The limited contact areas and rough surface morphology of the yarns lead to relatively poor bonding at the textile-LM interfaces. This weak bonding strength must then compete against the surface tension of the LM material during cyclic stretching. When the bonding is insufficient, the

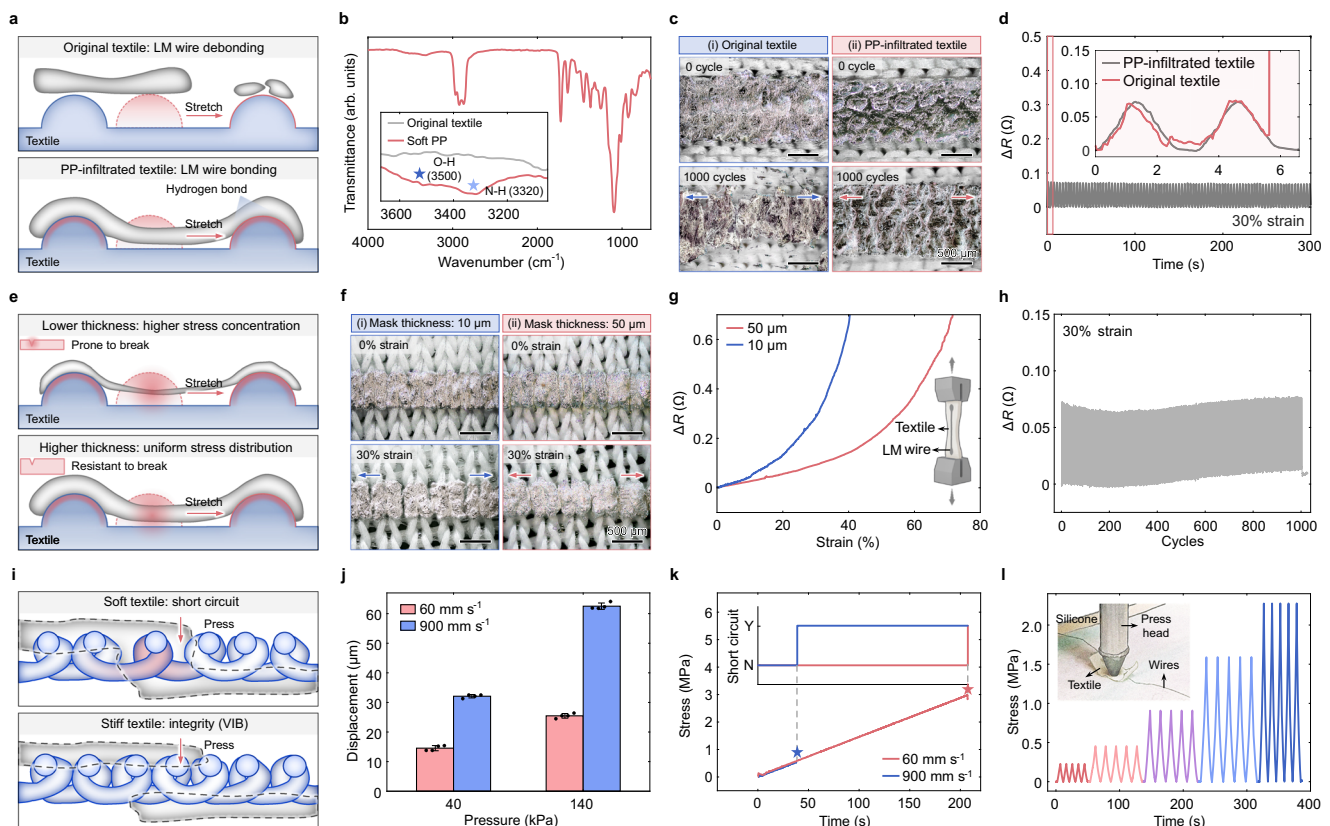


Fig. 3 | Stretchable and double-layer wires on LPT. **a** Schematics showing that PP-infiltrated textile surface stabilizes wire interfaces, while the original textile suffers from debonding at wire interfaces. The red semi-circle indicates the position of textile yarn before stretching. **b** FTIR spectra of the bulk PP from partial polymerization, with an inset highlighting the hydroxyl and amine stretching regions of both the PP and the original textile. **c** Photos of LM wires on different textile substrates before and after cyclic stretching. **d** Comparison between resistance variations of LM wires on original and PP-infiltrated textiles during cyclic stretching. **e** Schematics showing the effect of thickness of suspended LM wires on their resistance to break. The red semi-circle indicates the position of textile yarn before stretching. **f**, **g** (f) Photos and (g) resistance variations of stretched LM wires on textiles, which are fabricated using varied stencil masks. **h** Resistance variations of

an LM wire (length: 20 mm; width: 1 mm; mask thickness: 50 μ m) on a PP-infiltrated textile during 1000 stretch cycles. **i** Schematics showing that VIB induced by programmed stiffness prevents short circuits between LM wires on the opposite sides of textiles. In contrast, soft textiles develop vertical gaps under compressive strains, leading to cross-layer short circuits. VIB, vertical interconnect block. **j** Comparison between compressive displacements of PP-infiltrated textiles programmed at varied laser speeds. Laser power: 21.5 mW; Line spacing: 40 μ m. Error bars are presented as mean \pm SD for $n = 4$ independent experiments. **k** Compressive stress of VIBs produced by varied laser speeds, measured until short circuits occur. The marks indicate short circuits. Y: yes; N: no. Laser power: 21.5 mW; Line spacing: 40 μ m. **l** Compressive stress of a stiff VIB during cyclic pressing, and no short circuit occurs in the meantime.

surface tension beads up the LM material, inducing localized debonding and eventually fracture after stretching cycles³⁵. To address this issue, LPTs with PP on their surfaces provide high affinity to stabilize LM wires during stretching. Cross-sectional SEM images reveal fewer gaps between LM wires and PP-infiltrated textiles than in the case of original textiles (Supplementary Fig. 20f, g).

The LM affinity of PP-infiltrated textiles arises from surface chemistry and morphology. FTIR spectra confirm the presence O-H (3500 cm^{-1}) and N-H (3320 cm^{-1}) groups at the surface of PP (Fig. 3b). These functional groups form hydrogen bonds with the gallium oxide^{35,48} and also the gallium hydroxide⁴⁹ on the surface of LM wires, a capability absent in original textiles. Notably, this enhanced affinity is preserved even after post-polymerization washing and is independent of the polymerization degree of the PP (Supplementary Fig. 21), making it a practical strategy for improving the textile–LM interface. Moreover, PP may smooth the microscopic surface of fibers, potentially enhancing their contact with LM^{50,51} (Supplementary Fig. 22). In this way, PP-infiltrated textiles exhibit better affinity with LM wires, as evidenced by a contact-separation test (Supplementary Fig. 23). This affinity contributes to the stretch stability of LM wires on textiles, as the LM wire on the PP-infiltrated textile maintains smooth boundary even after 1000 cycles of 30% strain (Fig. 3c). In contrast, the LM wire on the original textile suffers from debonding and repeated friction with yarns during cyclic stretching. Thus, its boundary is heavily distorted. Resistance variations of both LM wires during cyclic stretching further demonstrate the superiority of the LPT, as the LM wire on the original textile becomes electrically disconnected in the second cycle (Fig. 3d). In contrast, the LM wire on the PP-infiltrated textile endures stretching with resistance variations below $0.1\ \Omega$. It is worth noting that the soft PP is specially programmed for this purpose using a laser speed of 900 mm s^{-1} , to keep the ductility of LPT–LM interface.

The unique physical properties of the LM paste further contribute to the stability of LM/textile interfaces. This intermetallic compound composed of CuGa_2 particles dispersed in a eutectic gallium–indium (EGaln) matrix exhibits internal particle-to-particle friction and wrinkled surface²⁸. The friction damps the fluidity of LM, leading to a significantly reduced surface tension. Additionally, the superficial wrinkles provide a higher oxide content than pristine LM surfaces, thereby promoting stronger hydrogen bonding with textiles. Consequently, the LM paste readily conforms to textile structures and remains bonded under dynamic stretching. Experimental results demonstrate that the pristine LM, even when printed on PP-infiltrated textiles, tends to bead up, debond, and eventually break after cyclic stretching (Supplementary Fig. 24). In contrast, the LM paste maintains its structural integrity under the same conditions. Thus, the use of LM paste for LM wires on textiles is practically meaningful.

The thickness of LM wires on textiles plays a crucial role in stretch stability. The suspended portions of LM wires between yarns are prone to break due to stress concentration at geometric defects (Fig. 3e). Finite element analysis (FEA) reveals that the wires with the larger thickness are less sensitive to stress concentration (Supplementary Fig. 25). Since LM wires are printed by stencil masks, their thickness can be roughly controlled by employing stencil masks of varied thickness (Supplementary Fig. 26). Under 30% strain, several cracks appear in the suspended regions of the LM wire printed by the $10\ \mu\text{m}$ -thick mask (Fig. 3f). In comparison, the LM wire printed by the $50\ \mu\text{m}$ -thick mask remains mostly connected under 50% strain (Supplementary Fig. 27). The thicker LM wire also exhibits the smaller resistance variations during stretching compared to its thinner counterpart (Fig. 3g). Thus, the relatively thick LM wire is preferred on textile surfaces as interconnections. However, excessively thick LM wires cannot be printed with desirable resolution (Supplementary Fig. 28). Hence, $50\ \mu\text{m}$ is the preferred mask thickness for LM wires on LPTs, and these wires are electrically stable under 1000 stretch cycles

(Fig. 3h). The resistance variation remains below $75\ \text{m}\Omega$ throughout stretching, with a baseline drift of less than $12\ \text{m}\Omega$.

Endurance to perpendicular pressure is important for the reliability of LM wires in real-world deformation conditions. On both rigid and soft supports, the LM wires exhibit no significant increase in resistance under pressure up to $\sim 3\ \text{MPa}$, which can be attributed to the intrinsic ductility of the LM paste (Supplementary Fig. 29). In addition, the minimum allowable width of LM wires is investigated from the perspective of stretch stability (Supplementary Fig. 30). Wires with widths of $500\ \mu\text{m}$ and wider withstand over 100% strain, a level sufficient for daily use⁵². However, at $250\ \mu\text{m}$, sample-to-sample deviation increases significantly. Based on these observations, $500\ \mu\text{m}$ is established as the minimum feasible width of LM wires on textiles. Given sufficient margin in the circuit layout, the line width can be increased up to 1 mm to further reduce resistance variation.

In addition to single-layer LM wires, double-layer LM wires and circuitry are greatly essential for high-density electronic systems. For porous substrates like textiles, external pressure can locally widen the vertical gaps by opening slip knots, resulting in cross-layer short circuits of LM pastes and posing critical electrical failures (Fig. 3i). The LPT with stiff VIBs located at the overlapping regions of front and back LM layers, effectively mitigates compressive strain and prevents cross-layer leakage of LM pastes. Since the effectiveness of VIBs is closely associated with their compressive stiffness, compressive characteristics of the LPT are studied. Under identical loading conditions, the compressive displacements of stiff LPT fabricated at a laser speed of 60 mm s^{-1} are less than half that of soft LPT produced at 900 mm s^{-1} (Fig. 3j and Supplementary Fig. 31a, b). When applying gradually increased stress onto overlapping LM wires on LPTs, a short circuit occurs at approximately $0.54\ \text{MPa}$ for the fully soft LPT, whereas the LPT with a stiff VIB withstands up to $-2.98\ \text{MPa}$ before failure (Fig. 3k). Even under repeated pressure cycles ranging from 0.25 to over $2\ \text{MPa}$ (Fig. 3l), as well as impacts that raise the stress by $1.9\ \text{MPa}$ within $-10\ \text{ms}$ (Supplementary Fig. 31c, d), the LPT with a VIB remains free from short circuits. Considering the maximum pressure applied by a human finger ($-0.2\ \text{MPa}$)⁵³ and the pressure involved when printing LM wires, the robust laser-programmed VIBs effectively protect textile circuits from electrical failures.

Gradient stiffness for strain isolation between LPT and chips

The LPTHE consists of the LPT, printed LM wires and chips interfacing with those wires. However, the modulus mismatch between the rigid chips and soft LPT–LM interfaces results in the debonding of stretched wires from the chip terminals (Fig. 4a). By programming gradient stiffness at the LPT–chip interfaces, strain isolation is achieved between the stretched LM wires and chip terminals, thereby ensuring reliable electrical connection under strain. FEA simulates stretched LPTs with the footprint of an SOT-23-5 package under 50% strain (Fig. 4b). Without gradient stiffness and strain isolation, the LPT with programmed soft regions undergoes visible deformation at the chip footprint. In contrast, additionally programming a stiff region at the chip footprint significantly reduces local strain. Experimental results further validate the effect of strain isolation. Before assembling chips onto LM wires, chip terminals are wetted with EGaln to establish a robust electrical connection to LM/Cu intermetallics in the LM wires (Supplementary Fig. 32). When a chip is assembled onto an LPT without strain isolation, the outlined terminal detaches from the LM wire under strain, and all the LM wires obviously expand along the direction of applied strain (Fig. 4c). This detachment may also lead to misalignment between chips and their footprints (Supplementary Fig. 33). In contrast, with strain isolation, all terminals maintain seamless contact with LM wires, and the wires beneath chip terminals exhibit no visible expansion (Fig. 4d). Therefore, the strain isolation contributed by LPTs reliably bridge textiles with rigid components.

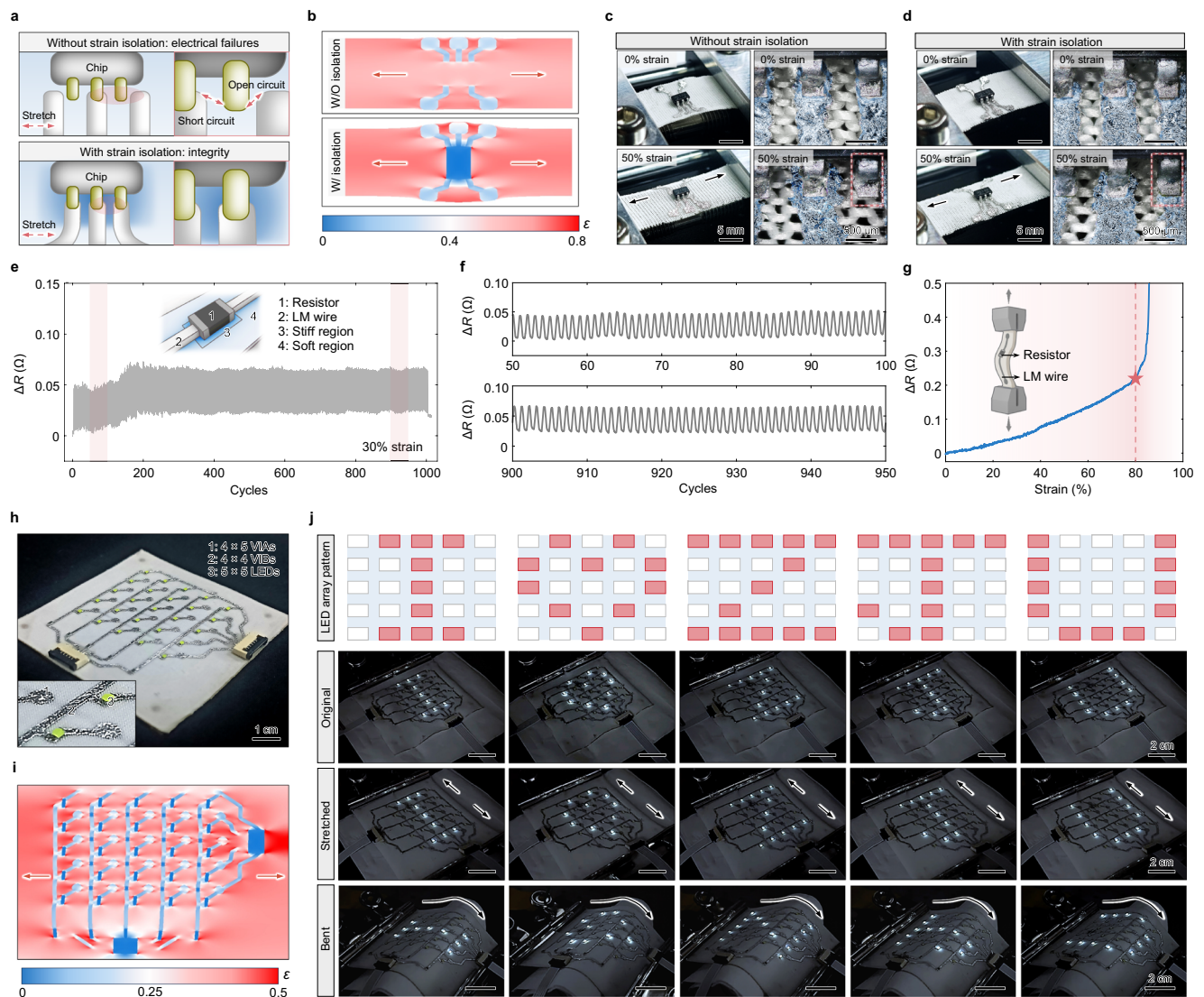


Fig. 4 | Stretchable LPTHE with gradient stiffness and strain isolation.

a Schematics showing that strain isolation induced by gradient stiffness (blue region) protects chips from open circuits and short circuits. For textiles without strain isolation, wires easily detach from chip terminals, and the lateral expansion of wires narrows the spacing between adjacent chip terminals. **b** FEA results showing the effect of gradient stiffness on strain distributions of textiles with an SOT-23-5 footprint. The LPT with only soft regions programmed cannot isolate strain and thus exhibits visible deformation at the chip footprint. For comparison, the LPT with gradient stiffness exhibits strain isolation, showing negligible strain in

the same area. **c, d** Photos of SOT-23-5 chips and LM wires on textiles (**c**) without and (**d**) with gradient stiffness. Both images are rendered using false colors. **e, f** (**e**) Resistance variations and (**f**) their enlarged view of an LPTHE resistor under cyclic stretching. **g** Resistance variations of the LPTHE resistor under gradually increased strain until failure. **h** Photos of a LPTHE screen containing 25 LED chips, 20 VIAs, and 16 VIBs. VIA, vertical interconnect access. **i** FEA results showing strain distributions of the substrate of the LPTHE screen. **j** Photos of the LPTHE screen displaying five different patterns when being stretched or bent.

To quantify the stability of strain isolation, a resistor of the 0603 package is assembled onto an LPT with a pair of LM wires and a central 0603 footprint. During 1000 stretch cycles, the resistance variation of entire component remains below 50 mΩ, with a baseline drift of less than 25 mΩ (Fig. 4e, f). Compared with the resistance variation of a single LM wire, the inclusion of a rigid component does not further increase the resistance change. Therefore, the electrical connections between the resistor and LM wires are not affected during stretching. Even under 80% strain, the chip terminals and LM wires are electrically connected, demonstrating robustness of this rigid–soft interface (Fig. 4g). Considering that the strains induced by typical motions of the human body are less than 55%⁵², this level of strain tolerance highlights the potential of the laser-programmed strain isolation as a reliable strategy for wearable textile hybrid electronics.

Demonstrations of the LPTHE systems

To demonstrate the capability of LPTHE for comparatively high-density electronics, an LPTHE screen is designed and fabricated on knitted textiles (Fig. 4h and Supplementary Fig. 34). The textile screen consists of a 5 × 5 array of white LEDs, and each of them can be independently addressed through the combination of its row and column. By sequentially switching the voltages of the front-row wires and back-column wires, various on-demand patterns can be displayed. To fabricate the LPT for this textile screen, 4 × 4 stiff VIBs are programmed at the intersections of row and column wires, and an additional 32 stiff regions are programmed at the footprints of chips (Supplementary Fig. 35a). Soft regions are programmed to seamlessly interface LM wires with the LPT. Owing to the porous nature of textiles, a laser scanning from the front side simultaneously polymerizes the PP on the back side. In this way, all the stiff and soft regions for front and back

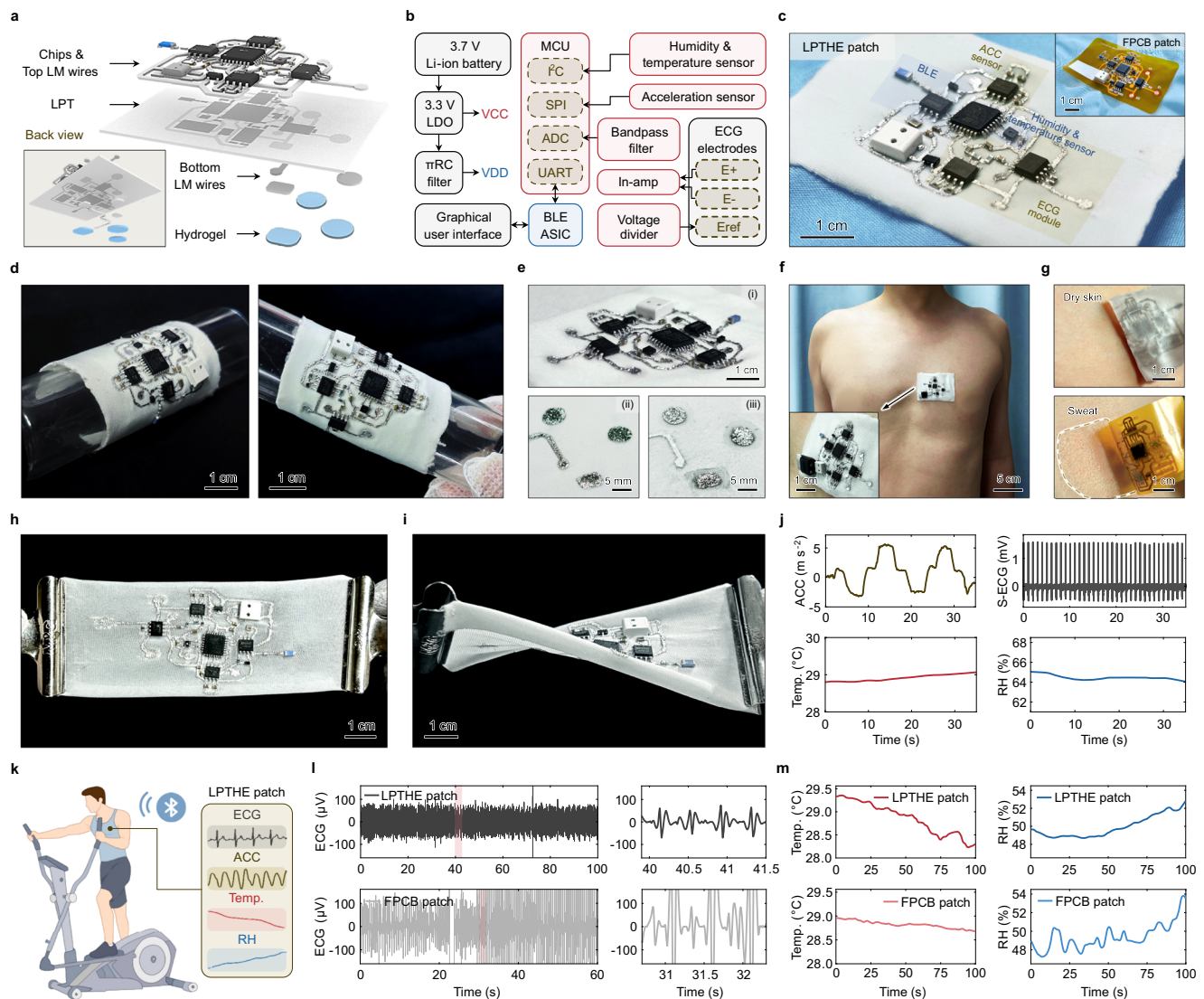


Fig. 5 | An LPTHE patch for continuous and multi-parameter health monitoring. **a** Exploded view of the LPTHE patch. **b** Functional block diagram of the LPTHE patch. LDO, low dropout regulator; BLE, Bluetooth low energy; ASIC, application-specific integrated circuit; UART, universal asynchronous receiver transmitter; ADC, analog-to-digital converter; SPI, Serial peripheral interface; I²C, inter-integrated circuit bus; In-amp, instrumentation amplifier. **c** Photo of the LPTHE patch with its FPCB counterpart in the inset. **d** Photos of the LPTHE patch bent along the surface of a cylinder with a 27 mm diameter. **e** Photos of the LPTHE patch showing its (i) front side, (ii) back side without encapsulation and (iii) back side with

encapsulation. **f** Photos of the LPTHE patch on the left chest of a volunteer. **g** Photos of human skin after exercising with the LPTHE patch and the FPCB patch, respectively. **h, i** Photos of the LPTHE patch under (h) ~40% strain and (i) twisting. **j** Multiple signals measured using the LPTHE patch during cyclic twisting. ACC: acceleration; S-ECG: simulated ECG. **k** Schematic of the LPTHE patch worn on a volunteer for real-time monitoring during exercise. **l, m** Comparison between the LPTHE patch and the FPCB patch in measuring (l) ECG signals and (m) temperature/humidity signals.

components can be programmed using a single laser scanning (Supplementary Fig. 35b, c). Furthermore, LM wires and 4×5 vertical interconnect accesses (VIAs) are printed on the LPT (Supplementary Fig. 35d). The stencil masks are machined in situ over the LPT to ensure precise alignment with laser-programmed patterns (Supplementary Fig. 36). VIAs with a diameter of 2.5 mm are located at the intersections between back and front wires in soft regions. Due to the porous and soft nature of these regions, VIAs can be simply activated by compressing the LM wires there, where the LM pastes permeate into the textile and form a vertical electrical connection. Finally, LEDs and other chips are aligned and mounted onto the stiff regions corresponding to their footprints, connected with front LM wires.

FEA simulates the strain isolation of the LPT in the textile screen (Fig. 4i). Under 30% strain, the footprints of rigid chips exhibit significantly lower strain levels than other regions of the LPT (Fig. 4j).

When the textile screen is connected to a driving circuit, five patterns ('I', 'love', 'Z', 'J', 'U') are sequentially displayed, even under bending and stretching (Fig. 4j).

To showcase the capability of LPTHE for wearable electronics, an untethered LPTHE patch is developed for multi-parameter health monitoring (Fig. 5a). The LPTHE patch integrates a single-lead ECG sensor, a z-axis acceleration sensor and a combined humidity-temperature sensor (Fig. 5b and Supplementary Fig. 37). These four health signals are transmitted via Bluetooth to a user interface. The LPT within the LPTHE patch is also elaborately programmed to interface rigid chips and double-layer LM wires (Supplementary Fig. 38). A photo of the fully assembled, monolithic LPTHE patch is illustrated (Fig. 5c). The patch is sufficiently ductile to conform to curved surfaces (Fig. 5d). To avoid short circuits between the back wires to curved surfaces, as well as contact contamination, a thin layer of poly(styrene-block-

butadiene-block-styrene) (SBS) fiber mat is electrospun onto the bottom surface of the LPTHE patch (Fig. 5e). This porous encapsulation is sweat-repellent, as indicated by a high contact angle ($\sim 130^\circ$), and is therefore intended to shield the patch from liquid perspiration (Supplementary Fig. 39). To acquire ECG signals, the mat is selectively removed to expose ECG electrodes to the skin.

The intrinsic permeability of LPTs, along with their fibrous encapsulation, enables the penetration of air and vapor. Even in regions covered by chips, air and vapor redirect laterally through the porous network of textiles and eventually exit beyond the boundaries of chips (Supplementary Fig. 40). The LPTHE patch exhibits overall breathability, permitting the natural passage of water vapor (Supplementary Fig. 41). In a practical scenario, the LPTHE patch is positioned on the left chest of a volunteer, with its corners secured using medical adhesive tape (Fig. 5f). After 10 minutes of exercise, the skin beneath the patch remains dry, indicating that sweat has evaporated through the permeable LPTHE (Fig. 5g). In contrast, when wearing a commercial flexible printed circuit board (FPCB) of the same design, which lacks permeability, sweat accumulates on the skin surface. This comparison highlights the superior wearing comfort of LPTHE. The mechanical stability of the LPTHE patch is validated under dynamic stretching and twisting (Fig. 5h, i and Supplementary Movie 2). Throughout these tests, a graphical user interface (GUI) manages data collection, online calculation and visualization (Supplementary Fig. 42). Remarkably, continuous signals are collected during these deformations, even under strains up to 50% (Fig. 5j and Supplementary Fig. 43). These results underscore the robustness of LPTHE for versatile electronic systems.

The permeable, stretchable and monolithic LPTHE patch enables real-time health monitoring during dynamic exercise (Fig. 5k and Supplementary Movie 3). The ECG signals acquired by the LPTHE patch exhibit clear waveforms and regular rhythm when the volunteer exercises on an elliptical machine (Fig. 5l). The heartrate derived from the ECG signals gradually increases and then saturates, indicating the adaptation and adjustment of a healthy cardiovascular system (Supplementary Fig. 44a). In contrast, the ECG signals of the FPCB patch exhibit significant noise at around 30th seconds, beyond which no identifiable characteristic peaks are observed. This failure results from the delamination of the non-stretchable substrate from the skin, as the skin itself undergoes dynamic expansion and contraction. During exercise, the acceleration signals display cyclic peaks corresponding to the vertical motion of the volunteer (Supplementary Fig. 44b, c). Step number and step frequency are derived from these acceleration signals, indicating consistent exercise intensity. The temperature and humidity signals acquired during exercise also reflect the distinct properties of the LPTHE. For this textile patch, the measured humidity gradually increases due to sweat evaporation, leading to body cooling as reflected by the decreased temperature (Fig. 5m). The intimate contact between the textile substrate and skin facilitates heat transfer. Moreover, the permeable textile substrate allows sweat vapor to pass from the skin to the humidity sensor, located on the opposite side of the substrate. However, for the non-stretchable FPCB patch, it struggles to conform to the skin, which is intrinsically a non-developable surface. The air gap between the skin and the FPCB patch hinders heat transfer, resulting in a smaller temperature decrease. At the same time, impermeable FPCB impedes the natural evaporation of sweat, leading to less stable humidity fluctuations. Hence, the LPTHE provides a more reliable and comfortable solution for health monitoring in practical scenarios.

Discussion

The mechanical mismatch between elastic textiles and hybrid electronic components is the primary obstacle to the development of stretchable hybrid electronics on textiles. Apart from using special

solder materials, engineering the textile itself is a straightforward strategy to surmount electrical and mechanical failures at heterogeneous interfaces. This work leverages the controllable photochemical reactions of PP at textile surfaces, which can be induced by regulated laser fluences. Through laser programming, the degree and region of the polymerization of PP in textiles can be customized. These LPTs exhibit finely tuned stiffness for strain isolation and for preventing cross-layer short circuits. Additionally, chemical groups on LPTs enhance the bonding of LM wires, significantly promoting the stretch stability of the LPTHE. In sum, the strategy proposed in this work is effective for stretchable textile hybrid electronics, and we envision that it can be extended to textiles with different weaving methods and also a broad range of PP. By developing PP with higher stiffness, as well as enhanced stretch recovery under partial polymerization, the stretchability and mechanical stability of LPTHE will be further improved. To address challenges in long-term wearability, the integration of directional wettability into LPTHE holds great promise, offering both wearing comfort and protection for electronics^{40,54}. Furthermore, the current method of securing the patch with adhesive tape may be insufficient for high-intensity activities. Future efforts will explore integrating LPTHE directly into full-body garments, providing a more reliable solution for dynamic applications.

Methods

Materials for fabricating the LPT and LPTHE

All processing solvents were used without further purification. Weft knitted textile (187#, Pedestrians Digital), PP precursors (H827, QUINSON, China) and UV glues (H806, QUINSON, China) were used as received. EGaln (melting point 15.7 °C, Dongguan Dingguan Metal Technology Co., Ltd., China) and Cu particles (99.98%, 0–10 μm , aladdin) were used in their original form. SBS (Kraton 1101), N,N-Dimethylformamide (DMF, aladdin) and tetrahydrofuran (THF, Macklin) were employed as supplied. Hydrogel slices were obtained from Omori Biological Technology Co., Ltd (Shenzhen, China).

Fabrication of the LPT and LPTHE

A UV lamp (wavelength: 365 nm, maximum power: 120 W) was utilized to process the PP-infiltrated textiles only for the samples in Fig. 2a–d and Supplementary Fig. 6. All bulk PP in this work was processed using the same lamp.

The fabrication of LPT began with infiltrating textiles with selective amounts of PP precursor using SLR (Supplementary Fig. 4, 5). Next, the textile was selectively processed by a UV nanosecond laser (355 nm wavelength, FOTIA-355-5-30-W, INNO Laser, China) to get an LPT. The laser beam was driven by a 2-axis galvo scanner (MOVIA, Novanta) and focused at a beam radius of around 9.5 μm . After laser scanning, the LPT was cleaned with IPA at room temperature using ultrasonic bath (1 minute) followed by magnetic stirring (2 hours, 500 rpm). The cleaned LPT was dried at 50 °C for 15 minutes.

LM pastes in this work were LM/Cu intermetallics. This intermetallic compound was synthesized by mixing EGaln with Cu particles at a mass ratio of 40:1 inside a high-speed planetary centrifugal mixer (AR100, Thinky) for 5 minutes. LM wires were printed on LPTs using customized water release stencil masks (thickness: $\sim 50 \mu\text{m}$). Water release stencil masks were prepared by laminating water-soluble tapes with polyimide tapes, followed by laser patterning. During printing, a flat-tip tweezer was used to rub the LM paste back and forth to infiltrate mask slots and wet the LPTs. After printing LM wires on LPTs, these stencil masks were removed in water, and LPTs with LM wires were dried (50 °C, 30 minutes). Other kinds of stencil masks include laser-patterned polyethylene terephthalate (PET) tapes (thickness: $\sim 10 \mu\text{m}$) and laser-patterned fabric tapes (thickness: $\sim 100 \mu\text{m}$). VIAs were formed by simply compressing front LM wires, where LM pastes permeated inward the soft regions of LPTs and formed electrical connection with back wires.

The LM wires at the textile-skin interface were encapsulated by electrospun SBS fiber mat (Supplementary Fig. 39). The solution for electrospinning was prepared by adding 14 wt% SBS into a mixed solvent (weight ratio of THF/DMF = 3:1). The voltage was set as 15 kV, the feeding rate was 9 mL h⁻¹, and the collecting distance was 20 cm. During electrospinning, the fiber mat inevitably encapsulated LM electrodes as well, which should have been exposed. To expose LM electrodes, this encapsulation was partially removed by a soldering iron at 200 °C.

To install chips on LM wires, both the chips and EGaln LM were first immersed in an 8 wt% sodium hydroxide (NaOH) solution (Supplementary Fig. 32). Bringing LM and chip terminals into contact under this condition formed metallic alloys at their interfaces. After all terminals were selectively corroded, chips were taken out from NaOH solution and carefully cleaned by cleanroom wipers. Next, chips were placed on LM wires in the right order. To reinforce the adhesion between chips and LPTs, corners of chips were fixed on LPTs by a UV glue (H806, QUINSON, China). The top side of the LPTHE was unencapsulated to facilitate clear visualization in experiments.

Characterizations of the LPT and LPTHE

Quasi-static mechanical properties of textiles were characterized and measured using a tensile apparatus (34sc-05, Instron). Impacts onto textiles were applied by a linear motor (DA60-BI-T60-CO10-0.2, Dynamikwell Technology, China), and meanwhile stress was measured using a pressure sensor (DYM105, Daysensor, China) beneath textiles. FTIR spectra were measured using an FT-IR Spectrometer (Nicolet 6700, Thermo Fisher Scientific). Air permeability was measured using an air permeability tester (YG461E, Wenzhou Jigao Testing Instrument Co., Ltd.) under the ASTM D737 standard (airflow pressure, 125 Pa). Water vapor permeability of LPT was measured over 15 days using the cup method according to the ASTM E96/E96M-13 standard at around 24 °C and 65% relative humidity. The moisture transmission rate was determined by measuring the weight loss of the water vapor in a cup with its opening firmly covered by the tested specimen. To characterize the water vapor permeability of the LPTHE, a beaker (opening diameter: 40 mm) containing boiling water was sealed with the LPTHE. The beaker was placed on a hot plate to maintain the water temperature.

Cytotoxicity was reflected by cell viability, which was assessed by CCK-8 assay of L929 fibroblasts (STM-CL-6929, Stem Recell, China) after 24 hours exposure to 100% extracts of textiles. Cells were maintained in Minimum Essential Medium (MEM, BR3000034, Bioleaper, China) supplemented with 10% fetal bovine serum (FBS, STM-CM-0102, Stem Recell, China) and 1% penicillin-streptomycin (P/S, BR3001460, Bioleaper, China). Each sample was measured three times and averaged. Fluorescent images were captured using an inverted fluorescence microscope (DSZ2000X, Chongqing UOP Optoelectronic Technology Co., Ltd) after staining with a Calcein-AM/PI double-staining kit (C2015, Beyotime, China).

The intensity of laser power was measured using a commercial power meter (843-R, Newport) with a probe (919P-150-26, Newport), as illustrated in Supplementary Fig. 12a. Electrical resistances of LM wires and circuits were measured using a digital multimeter (34470 A, Keysight) with Kelvin clamps. Topographies of LM wires were measured using a confocal scanning laser microscope (VK-X100, Keyence Corporation, Japan). Copper wires at a diameter of 100 μm connected Kelvin clamps with measured objects. When acquiring health signals from the volunteer, the corners of the LPTHE patch were stuck to the skin by medical adhesive tape. The simulated ECG waveform was produced by the voltage drop across the V3 and V4 terminals of an ECG simulator (SKX-2000C, Ming Sheng, China). Artificial sweat with the PH value of 6.5 was utilized to evaluate the waterproofness of the fiber encapsulation (YT-001, Yangtuo, China).

To characterize PP precursor, NMR spectroscopy was measured using an NMR spectrometer (Avance NEO 400, Bruker). ¹H NMR spectra were acquired at 400.15 MHz with a relaxation delay of 1.00 s. ¹³C NMR and ³¹P NMR spectra were acquired at 100.63 MHz and 161.98 MHz, respectively, both using a relaxation delay of 2.00 s. All spectra were measured in dimethyl sulfoxide-d₆ (DMSO-d₆). Gas chromatographic mass spectrometry was conducted using a gas chromatograph system (Agilent 8860, Agilent Technologies) equipped with a mass selective detector (Agilent 5977B, Agilent Technologies). Pyrolysis gas chromatographic mass spectrometry was conducted using a gas chromatograph system (GCMS-QP2020 NX, Shimadzu), and samples were pyrolyzed at 600 °C using a multishot pyrolyzer (EGA/PY-3030D, Frontier Laboratories). XRF spectrum was measured using an XRF spectrometer (ZSX Primus III NEXT, Rigaku).

Simulations for the LPT

FEA analyses were conducted using COMSOL Multiphysics 6.1. Textiles in FEA were modeled as nonlinear elastic materials, whose strain-stress relations were derived from Fig. 2l (thickness approximated as 400 μm). FDTD analyses were conducted using ANSYS Lumerical 2024 R1. The waist radius of Gaussian beam was 9.5 μm. The thickness of plane and the diameter of fibers are 8 μm and 10 μm, respectively. The refractive index of both the plane and fibers was set as 1.67.

Electronic systems for the LPTHE

All resistors, capacitors and LEDs in this work employed the 0603 package. The LPTHE screen was driven by an Arduino Uno development board. A laptop received data packages from the LPTHE patch through a BLE-to-UART module (doBT-M01, doiot). Each data package consisted of 60 ECG samples, nine acceleration samples, one temperature sample and one humidity sample, at a transmission speed of six packages per second. When wearing the LPTHE patch, the measurement axis of the acceleration sensor was aligned along the vertical direction, with the positive direction pointing upward. The built-in high-pass filter in the acceleration sensor removed the bias signal induced by gravity.

Graphical user interface

The GUI for the LPTHE patch was designed using App Designer, MATLAB 2023a. The GUI captured, filtered, calculated and visualized real-time signals. The visualized ECG signals were subject to a median filter (order: 13) and then a mean filter (order: 7). The step number was calculated from the acceleration signals using a median filter (order: 5) and peak detection algorithm (threshold: ±0.58 m s⁻²).

Data processing

Young's moduli were calculated through linear regressions of strength-strain curves within the range from 0 to 20% strain. Toughness was calculated as the areas between strength-strain curves and the strain axis within the range from 0 to 20% strain. ECG, acceleration, temperature and humidity were sampled at 360 Hz, 54 Hz, 6 Hz, and 6 Hz, respectively. The plotted ECG signals and acceleration signals were subject to a median filter (order: 13) and then a mean filter (order: 7). The plotted temperature signals and humidity signals were subject to a median filter (order: 17) and then a mean filter (order: 9). The instantaneous heart rate signals were derived by inverting the R-R interval (*i.e.*, the time elapsed between two adjacent R waves) of ECG signals, followed by a median filter (order: 3) and then a mean filter (order: 5). R waves were found by searching data points that were locally maximum within 0.33 s from each of them. The instantaneous step frequencies were calculated as the average rate of change in step numbers within the past four seconds. False colors in SEM images were created by Adobe PhotoShop CC 2018.

Experiments on human subjects

The experiments were performed in compliance with the protocol approved by the ethical committee of College of Biomedical Engineering and Instrument Science, Zhejiang University ((2024)-7). A single 27-year-old male volunteer was recruited for the proof-of-concept demonstration in related experiments, and informed consent was obtained from him. The conclusions derived from human subject studies are qualitative, sex-independent, and thus applicable to both male and female participants.

Statistical information

Discrete experimental data were statistically analyzed, and the results are expressed as mean \pm standard deviation. These measurements were taken from distinct sample. MATLAB 2023a was used for data analysis.

Reporting summary

Further information on research design is available in the Nature Portfolio Reporting Summary linked to this article.

Data availability

The raw and processed data related to this study are provided in the Source data file. Source data are provided with this paper.

References

1. Wang, Z., Liu, Y., Zhou, Z., Chen, P. & Peng, H. Towards integrated textile display systems. *Nat. Rev. Electr. Eng.* **1**, 466–477 (2024).
2. Wu, W. & Lee, P. S. Flexible and stretchable electrochromic displays: strategies, recent advances, and prospects. *Soft Sci.* **4**, 29 (2024).
3. Tian, X. et al. Wireless body sensor networks based on metamaterial textiles. *Nat. Electron.* **2**, 243–251 (2019).
4. Ye, L. et al. A rechargeable calcium–oxygen battery that operates at room temperature. *Nature* **626**, 313–318 (2024).
5. Chen, G., Li, Y., Bick, M. & Chen, J. Smart textiles for electricity generation. *Chem. Rev.* **120**, 3668–3720 (2020).
6. Xu, G. et al. Self-powered electro-tactile textile haptic glove for enhanced human-machine interface. *Sci. Adv.* **11**, eadt0318 (2025).
7. Wei, X. et al. Multimodal electronic textiles for intelligent human-machine interfaces. *Soft Sci.* **3**, 17 (2023).
8. Zeng, Q. et al. A digitally embroidered metamaterial biosensor for kinetic environments. *Nat. Electron.* **7**, 1025–1034 (2024).
9. Yan, W. et al. Single fibre enables acoustic fabrics via nanometre-scale vibrations. *Nature* **603**, 616–623 (2022).
10. Libanori, A., Chen, G., Zhao, X., Zhou, Y. & Chen, J. Smart textiles for personalized healthcare. *Nat. Electron.* **5**, 142–156 (2022).
11. Rajappan, A. et al. Logic-enabled textiles. *Proc. Natl. Acad. Sci. USA*. **119**, e2202118119 (2022).
12. Zheng, Y., Wang, Z., Chen, P. & Peng, H. Semiconductor fibers for textile integrated electronic systems. *Natl. Sci. Rev.* **11**, nwa143 (2024).
13. Wang, Z. et al. High-quality semiconductor fibres via mechanical design. *Nature* **626**, 72–78 (2024).
14. Chen, G. et al. Electronic textiles for wearable point-of-care systems. *Chem. Rev.* **122**, 3259–3291 (2022).
15. Wang, P. W. et al. Well-defined in-textile photolithography towards permeable textile electronics. *Nat. Commun.* **15**, 887 (2024).
16. Roh, J. S. All-fabric interconnection and one-stop production process for electronic textile sensors. *Text. Res. J.* **87**, 1445–1456 (2017).
17. Koshi, T., Nomura, K. & Yoshida, M. Electronic component mounting for durable E-textiles: direct soldering of components onto textile-based deeply permeated conductive patterns. *Micro-machines* **11**, 209 (2020).
18. Luo, H. et al. Textile hybrid electronics for monolithically multimodal wearable monitoring and therapy. *Int. J. Extrem. Manuf.* **7**, 035506 (2025).
19. Gupta, N. et al. A single-fibre computer enables textile networks and distributed inference. *Nature* **639**, 79–86 (2025).
20. Zhuang, Q. et al. Permeable, three-dimensional integrated electronic skins with stretchable hybrid liquid metal solders. *Nat. Electron.* **7**, 598–609 (2024).
21. Zheng, S. et al. Pressure-stamped stretchable electronics using a nanofibre membrane containing semi-embedded liquid metal particles. *Nat. Electron.* **7**, 576–585 (2024).
22. Ai, L. et al. “Heat-Press-N-Go” stretchable interconnects enabled by liquid metal conductor with supramolecular confinement. *Adv. Funct. Mater.* **35**, 2425264 (2025).
23. Li, Y., Veronica, A., Ma, J. & Nyein, H. Y. Y. Materials, structure, and interface of stretchable interconnects for wearable bioelectronics. *Adv. Mater.* **37**, 2408456 (2025).
24. Guo, R. et al. Semiliquid metal enabled highly conductive wearable electronics for smart fabrics. *ACS Appl. Mater. Interfaces* **11**, 30019–30027 (2019).
25. Zhang, T., Asher, E. & Yang, J. A new printed electronics approach eliminating redundant fabrication process of vertical interconnect accesses: building multilayered circuits in porous materials. *Adv. Mater. Technol.* **3**, 1700346 (2018).
26. Kim, I., Ju, B., Zhou, Y., Li, B. M. & Jur, J. S. Microstructures in all-inkjet-printed textile capacitors with bilayer interfaces of polymer dielectrics and metal–organic decomposition silver electrodes. *ACS Appl. Mater. Interfaces* **13**, 24081–24094 (2021).
27. Decker, C. Kinetic study and new applications of UV radiation curing. *Macromol. Rapid Commun.* **23**, 1067–1093 (2002).
28. Tang, J. B. et al. Gallium-based liquid metal amalgams: transitional-state metallic mixtures (TransM²ixes) with enhanced and tunable electrical, thermal, and mechanical properties. *ACS Appl. Mater. Interfaces* **9**, 35977–35987 (2017).
29. Liu, S., Shah, D. S. & Kramer-Bottiglio, R. Highly stretchable multi-layer electronic circuits using biphasic gallium-indium. *Nat. Mater.* **20**, 851–858 (2021).
30. Ai, L. et al. Tough soldering for stretchable electronics by small-molecule modulated interfacial assemblies. *Nat. Commun.* **14**, 7723 (2023).
31. Lopes, P. A., Santos, B. C., de Almeida, A. T. & Tavakoli, M. Reversible polymer-gel transition for ultra-stretchable chip-integrated circuits through self-soldering and self-coating and self-healing. *Nat. Commun.* **12**, 4666 (2021).
32. Lee, S. G. et al. Mechanically stable, and reversible integration of microchips on textile: liquid metal-based anisotropic conductive adhesive. *npj Flex. Electron.* **9**, 72 (2025).
33. Shao, Y. et al. A universal packaging substrate for mechanically stable assembly of stretchable electronics. *Nat. Commun.* **15**, 6106 (2024).
34. Kim, M. et al. A gradient stiffness-programmed circuit board by spatially controlled phase-transition of supercooled hydrogel for stretchable electronics integration. *Adv. Mater.* **36**, 2313344 (2024).
35. Liu, X. et al. Stiffness and interface engineered soft electronics with large-scale robust deformability. *Adv. Mater.* **36**, 2407886 (2024).
36. Zhao, Y., Pei, D., Zhou, C., Liang, K. & Li, Y. A programmable stiffness substrate with high modulus contrast and high-resolution patterns for strain-insensitive stretchable electronics. *Chem. Eng. J.* **505**, 159728 (2025).
37. Tang, L., Wang, H., Ren, J. & Jiang, X. Highly robust soft-rigid connections via mechanical interlocking for assembling ultra-stretchable displays. *npj Flex. Electron.* **8**, 50 (2024).
38. Wang, D. et al. Recent advances on additive manufacturing of heterogeneous/gradient metallic materials via laser powder bed fusion. *Int. J. Extrem. Manuf.* **7**, 062007 (2025).
39. Ge, Q. et al. Projection micro stereolithography based 3D printing and its applications. *Int. J. Extrem. Manuf.* **2**, 022004 (2020).

40. Das, B., Das, A., Kothari, V. K., Fanguiero, R. & Araújo, M. D. Moisture transmission through textiles. *Autex Res. J.* **7**, 100–110 (2007).
41. Singal, K. et al. Programming mechanics in knitted materials, stitch by stitch. *Nat. Commun.* **15**, 2622 (2024).
42. Ahmed, N., Darwish, S. & Alahmari, A. M. Laser ablation and laser-hybrid ablation processes: a review. *Mater. Manuf. Process.* **31**, 1121–1142 (2016).
43. Decker, C. & Moussa, K. Kinetic investigation of photopolymerizations induced by laser beams. *Macromol. Chem. Phys.* **191**, 963–979 (1990).
44. James, J., Annamalai, A. R., Muthuchamy, A. & Jen, C.-P. Effect of wettability and uniform distribution of reinforcement particle on mechanical property (tensile) in aluminum metal matrix composite—a review. *Nanomaterials* **11**, 2230 (2021).
45. Chen, G. et al. Strengthening mechanisms based on reinforcement distribution uniformity for particle reinforced aluminum matrix composites. *Trans. Nonferrous Met. Soc. China* **28**, 2395–2400 (2018).
46. Taschner, R., Gauss, P., Knaack, P. & Liska, R. Biocompatible photoinitiators based on poly- α -ketoesters. *J. Polym. Sci.* **58**, 242–253 (2020).
47. Luo, Y. et al. Structural design and preparation of LED/moisture dual-cured polyurethane acrylate coatings with comprehensive properties. *Prog. Org. Coat.* **200**, 109080 (2025).
48. Zhang, Y. et al. Dynamic-wetting liquid metal thin layer induced via surface oxygen-containing functional groups. *ACS Nano* **19**, 4913–4923 (2025).
49. Jung, W. et al. Giant decrease in interfacial energy of liquid metals by native oxides. *Adv. Mater.* **36**, 2406783 (2024).
50. Joshipura, I. D. et al. Are contact angle measurements useful for oxide-coated liquid metals? *Langmuir* **37**, 10914–10923 (2021).
51. Ma, J. et al. Metallophobic coatings to enable shape reconfigurable liquid metal inside 3D printed plastics. *ACS Appl. Mater. Interfaces* **13**, 12709–12718 (2021).
52. Yamada, T. et al. A stretchable carbon nanotube strain sensor for human-motion detection. *Nat. Nanotechnol.* **6**, 296–301 (2011).
53. Xu, Y. et al. Porous liquid metal-elastomer composites with high leakage resistance and antimicrobial property for skin-interfaced bioelectronics. *Sci. Adv.* **9**, eadf0575 (2023).
54. Zhang, B. B. et al. A three-dimensional liquid diode for soft, integrated permeable electronics. *Nature* **628**, 84–92 (2024).

Acknowledgements

This work was supported by the Zhejiang Provincial Natural Science Foundation of China (LDQ24E050001, LR26E050002), the National Natural Science Foundation of China (U25A20321, 52475610), and “Leading Goose” R&D Program of Zhejiang (2023C03007, 2023C01051) granted to Kaichen Xu. The authors thank Menglian Zheng and Pengfei Wang from Zhejiang University for the help on device fabrication. The authors also thank Xi Zheng and Dongmei Qi from the Analysis Center of Agriculture, Life and Environment Sciences Zhejiang University for their technical assistance with SEM. The authors extend their gratitude to Ms. Wendi Chen (from Scientific Compass www.shiyanjia.com) for providing invaluable assistance with the NMR, GC–MS and XRF analysis.

Author contributions

H.Y.L. and Z.M.C. equally contributed to this work. H.Y.L. and K.C.X. conceived the idea. H.Y.L. and Z.M.C. carried out the device fabrication, characterizations and demonstrations. K.J.Y. and H.Y.L. designed the simulations and data processing algorithm. G.Y., J.T., Y.Z.h., H.Y.Y., K.W.N., and M.D.D. provided extensive suggestions on experimental designs and applications. T.L., H.L., Y.Zhang and H.X. helped with data analysis. H.Y.L. designed circuits and graphical user interfaces. Z.M.C. and H.Y.L. prepared data plots and figures. K.C.X. supervised the project. H.Y.L., Z.M.C., and K.C.X. wrote and revised the manuscript. All the authors discussed the results and commented on the manuscript.

Competing interests

K.C.X., H.Y.L., Z.M.C., G.Y., and H.Y.Y. are listed as the inventors of a Chinese patent filed for the LPTHE (2025113927663, 2025113927644). The authors declare no other competing interests.

Additional information

Supplementary information The online version contains supplementary material available at <https://doi.org/10.1038/s41467-025-67149-x>.

Correspondence and requests for materials should be addressed to Kaichen Xu.

Peer review information *Nature Communications* thanks Jaehong Lee, Xi Yao, and the other anonymous reviewer(s) for their contribution to the peer review of this work. A peer review file is available.

Reprints and permissions information is available at <http://www.nature.com/reprints>

Publisher’s note Springer Nature remains neutral with regard to jurisdictional claims in published maps and institutional affiliations.

Open Access This article is licensed under a Creative Commons Attribution-NonCommercial-NoDerivatives 4.0 International License, which permits any non-commercial use, sharing, distribution and reproduction in any medium or format, as long as you give appropriate credit to the original author(s) and the source, provide a link to the Creative Commons licence, and indicate if you modified the licensed material. You do not have permission under this licence to share adapted material derived from this article or parts of it. The images or other third party material in this article are included in the article’s Creative Commons licence, unless indicated otherwise in a credit line to the material. If material is not included in the article’s Creative Commons licence and your intended use is not permitted by statutory regulation or exceeds the permitted use, you will need to obtain permission directly from the copyright holder. To view a copy of this licence, visit <http://creativecommons.org/licenses/by-nc-nd/4.0/>.

© The Author(s) 2026